Chemical Science

EDGE ARTICLE

View Article Online
View Journal | View Issue

Cite this: *Chem. Sci.*, 2018, **9**, 3386

Tailored metastable Ce–Zr oxides with highly distorted lattice oxygen for accelerating redox cycles†

Zhe Zhang,‡[a] Jiafeng Yu,‡*[a] Jixin Zhang,[a] Qingjie Ge,[a] Hengyong Xu,[a] Felix Dallmann,[b] Roland Dittmeyer[b] and Jian Sun*[a]

Ceria-based catalysts are widely used in oxidation or oxidation–reduction reactions in the field of environmental science. Their catalytic functions are determined by their ability to exchange oxygen species with oxidants. The enhancement of oxygen release is desired since it is often the rate-determining step in redox cycles. Herein, we developed a lattice oxygen distortion method to enhance oxygen activation by quenching the Ce–Zr oxide nanoparticles formed from an extremely high temperature. This process can ensure the formation of solid solutions as well as avoiding atomic rearrangement during calcination, retaining the lattice oxygen at a metastable and disordered state without vacancies. Reduction, vacuum or metal deposition will easily induce oxygen release accompanied by vacancy creation. The metastable oxides can provide about 19 times more oxygen vacancies than traditional ones in a CO atmosphere. CO oxidation rates increased with increasing Zr content from 25 to 75% and achieved a new level, which is attributed to the acceleration of oxygen circulation *via* promoting oxygen release and supplying plenty of oxygen vacancies for redox cycles. This strategy is expected to be applied in the design and fabrication of improved oxygen storage materials.

Received 13th February 2018
Accepted 28th February 2018

DOI: 10.1039/c8sc00729b

rsc.li/chemical-science

Introduction

The development of three-way catalysts (TWCs) is desired due to the urgent requirement for eliminating the hydrocarbon, CO and NO_x pollutants in automotive exhaust. Ceria-based composites as typical TWCs are directly involved in this oxidation–reduction catalytic process as "active" components *via* exchanging oxygen species with oxidants.[1] They are widely used due to their essential role in supplying active oxygen species for oxygen activation and their ability to act as an oxygen buffer by storing/releasing O_2 due to the Ce^{4+}/Ce^{3+} redox couple.[2,3] Take CO oxidation for example, this activation process follows the MvK mechanism, where active lattice oxygen on the surface of an oxide is removed by reaction with CO, and the oxygen vacancies (OVs) are subsequently replenished by reaction with O_2 from the gas phase.[4,5] Isotopically labeled oxygen studies have also proved that the oxygen atom incorporated in the reactant is directly extracted from the solid surface rather than derived from the gas phase.[6] This redox cycle can be enhanced by accelerating the oxygen release since it is often the rate-determining step.

Recently, Safonova *et al.*[7] proposed that the activity in CO oxidation is independent of the oxygen storage capacity (OSC) and Ce^{3+} amount in the steady state. The release of oxygen atoms from the support which react with CO to form OVs and CO_2 has been identified as the rate-determining step. The dynamic oxygen mobility or oxygen diffusivity is related more closely to the oxygen release rate in practical catalytic processes. Moreover, Haruta *et al.*[8] observed a clear volcano-like correlation between the CO oxidation activity of oxides and their metal–oxygen binding energy (E_{M-O}). Oxides with low E_{M-O}, such as Fe_2O_3, may slow down the incorporation of oxygen from the gas phase into OVs, while for those with high E_{M-O}, such as CeO_2 and ZrO_2, it is hard to release oxygen. Therefore, decreasing E_{Ce-O} may be an effective way to enhance oxygen activation and accelerate redox cycles. This fact provides significant motivation for intense research in developing techniques which could weaken the Ce–O interaction to create active oxygen and promote oxygen release. For instance, placing the smaller Zr^{4+} (ionic radius of 0.84 Å) at the position of the larger Ce^{4+} (0.97 Å) disturbs Ce–O interactions, leading to a decrease in the local Ce–O coordination number from 8 to 7 and to the formation of structural defects.[9] Moreover, the formation of heterotypic ceria could change the surface Ce–O interaction through different exposed surface planes.[10,11] The Ce–O interaction is also related to the metal–oxide interface,

[a]*Dalian Institute of Chemical Physics, Chinese Academy of Sciences, Dalian, China. E-mail: yujf@dicp.ac.cn; sunj@dicp.ac.cn*

[b]*Institute for Micro Process Engineering, Karlsruhe Institute of Technology, Karlsruhe, Germany*

† Electronic supplementary information (ESI) available. See DOI: 10.1039/c8sc00729b

‡ These authors contributed equally to this work.

lattice strain and metastable t″ phase.[5,12,13] However, weakened Ce–O interactions would lead to oxygen release and oxygen vacancy formation during calcination treatment in traditional catalyst preparation methods, resulting in a loss of active oxygen. Therefore, how to create active oxygen species as much as possible and at the same time keep them stable until reaction becomes an intractable problem.

Flame spray pyrolysis (FSP) is a highly promising and versatile technique for the rapid synthesis of nanostructured materials without any subsequent calcination treatment. The combustion of aerosols at high temperature (*ca.* 2000 °C (ref. 14)) followed by rapid quenching (*ca.* 60 °C μs^{-1} (ref. 15)) produces highly dispersed nanosized oxide powders with metastable structures,[16–18] which may not be easily accessible by conventional processes.[19,20] Herein, we design a series of metastable Ce–Zr oxides by employing the FSP method. A strong correlation between the oxygen distortion and the redox properties of the studied Au/$Ce_{1-x}Zr_xO_2$ catalysts for a CO oxidation probe reaction has been established. Rapid quenching could inhibit atomic rearrangement and make the oxygen atoms stable at a highly disordered state. These oxygen atoms are active and readily released in the reaction atmosphere, solving the intractable problem mentioned above. The target of this work is to reveal the role of oxygen distortion in oxygen activation and the key factors determining oxygen release. It is expected to explore the potential of metastable oxides for enhancing oxygen activation and provide a new strategy for accelerating redox reaction rates.

Experimental

Materials preparation

The FSP samples were prepared by using the setup at the Karlsruhe Institute of Technology (KIT), which was described elsewhere.[21] Appropriate amounts of cerium(III) 2-ethylhexanoate (49% in 2-ethylhexanoic acid, 12% Ce) and zirconium(IV) 2-ethylhexanoate were dissolved in xylene to a final cerium and zirconium concentration of 0.5 M. The precursor was fed to the flame at 5 ml min^{-1} using a syringe pump (PHD Ultra™, Harvard) and dispersed by oxygen (feed rate 3.5 l min^{-1} and pressure 4.5 bar). The flame was ignited by premixed methane (0.6 l min^{-1}) and oxygen (1.9 l min^{-1}) issued from an annular gap. The product particles were collected on a water-cooled glass fiber filter (Whatman GF/D, 25.7 cm in diameter) with the help of a vacuum pump. A series of mixed oxides with different Ce/Zr molar ratios were synthesized by the above procedures and denoted as FSP-$Ce_{1-x}Zr_xO_2$ ($x = 0$, 0.25, 0.5, and 0.75). Thermal treatment was conducted for the FSP-$Ce_{0.25}Zr_{0.75}O_2$ sample at 800 °C for 30 h in air, which was then denoted as FSP-$Ce_{0.25}Zr_{0.75}O_2$–C.

For comparison, a series of the same ratio $Ce_{1-x}Zr_xO_2$ mixed oxides (denoted as CP-$Ce_{1-x}Zr_xO_2$, $x = 0$, 0.25, 0.5, and 0.75) were prepared by a traditional co-precipitation method (CP). Adequate amounts of ammonium cerium(IV) nitrate and zirconium(IV) nitrate were dissolved in deionized water to a final Ce and Zr concentration of 0.3 M. Then the $(NH_4)_2CO_3$ solution (0.6 M) was slowly added into the above solution at 50 °C with continuous stirring until the pH value reached 8–9. The solution was centrifuged and washed until pH = 7.0. The obtained precipitate was dried at 110 °C for 10 h and calcined in air at 500 °C for 4 h. The Zr content was determined by SEM-EDS.

Au was deposited onto supports *via* a deposition–precipitation (DP) method.[22] At room temperature, an adequate amount of $HAuCl_4 \cdot 4H_2O$ to obtain 1 wt% of gold was dissolved in 40 ml deionized water (6.0×10^{-4} M). The pH of the solution was adjusted to 9 by adding 0.1 M NaOH. Then 0.5 g support was added and the mixture was kept for 1 h under continuous stirring, maintaining the pH at around 9 *via* continuous NaOH addition. After that, the suspension was heated to 65 °C and stirred for 1 h in a water bath. The precipitates were filtered and washed with deionized water to eliminate Cl^-. The obtained solid was dried at 60 °C for 10 h and calcined in He (30 ml min^{-1}) at 300 °C for 2 h.

Characterization

Powder X-ray diffraction (XRD) patterns were recorded on an X'Pert Pro (PANAlytical) diffractometer with Cu Kα radiation at 40 kV and 40 mA over a 2θ range from 5 to 80°. The crystal grain size was calculated from the FWHM of the strongest (111) reflection according to the Scherrer equation. Both lattice parameters and lattice strain were calculated using the Scherrer equation based on the (111) and (101) reflections in space groups $Fm\bar{3}m$ and $P4_2/nmc$, respectively. Electron paramagnetic resonance (EPR) spectra were recorded with a Bruker A200 EPR spectrometer at 100 K. Equal amounts of the catalysts were placed into a homemade quartz tube with stopcocks. Transmission electron microscopy (TEM) images were obtained with a JEM-2100 system (JEOL) with an acceleration voltage of 200 kV. The samples were ultrasonically suspended in ethanol and dropped onto a carbon film supported over a Cu grid. Raman spectra were recorded on a commercial micro-Raman spectrometer (Renishaw, UK) using an Ar laser with a wavelength of $\lambda = 514$ nm working at 30 mW. *In situ* Raman spectra were obtained in a 2% CO/He or pure He (99.99%) atmosphere at 6 mW. The samples were heated from 25 to 300 °C with a temperature ramp rate of 10 °C min^{-1}. The data were collected after stabilization for 5 min at each temperature. Raman peak shifts and areas were determined by fitting to Lorentzian line shapes ($R^2 > 0.95$). X-ray photoelectron spectroscopy (XPS) was carried out to determine the surface compositions of the as-prepared catalysts with an ESCALAB 250Xi instrument using Al Kα radiation ($h\nu = 1486.6$ eV). The C1s peak was set at 284.6 eV and taken as the reference for binding energy calibration. Temperature programmed reduction with hydrogen (H_2-TPR) was carried out in a homemade setup with a conventional U-shaped quartz reactor connected to a thermal conductivity detector (TCD). 50 mg samples were loaded and pretreated in Ar (30 ml min^{-1}) at 300 °C for 0.5 h. The TPR was performed in 5% H_2/Ar (30 ml min^{-1}) from room temperature to 900 °C at a rate of 10 °C min^{-1}. The loading of Au was determined by inductively coupled plasma optical emission spectroscopy (ICP-OES). The samples (10–20 mg) were chemically digested by dissolution in a mixture of 12 ml HCl and 4 ml HNO_3 in an autoclave at 160 °C for 4 h.

Reaction tests

The CO oxidation reaction was executed in a fixed bed with 8 mm inner diameter under ambient pressure. A gas mixture containing 1.67 vol% CO, 3.33 vol% O_2 and 95 vol% He as balance was used with a flow of 37.5 ml min^{-1} for Au-based catalysts (25 mg) and 10 ml min^{-1} for the Ce–Zr oxide solid solution (50 mg). The CO conversion was measured in the temperature range of 25–100 °C for Au-based catalysts and 100–450 °C for the Ce–Zr oxide solid solution. The effluents from the reactor were analyzed using a gas chromatograph (Shimadzu GC-8A) equipped with a carbon molecular sieve column (TDX-1, Dalian Zhonghuida Scientific Instrument Co. Ltd) and a thermal conductivity detector (TCD). At each reaction temperature, the CO conversion was calculated based on the composition of the product gas after 1 h stabilization.

Results and discussion

Properties of the metastable Ce–Zr oxide solid solution

Here, a series of $Ce_{1-x}Zr_xO_2$ with a wide range of compositions (x = 0–0.75) were prepared by both FSP and co-precipitation (CP) methods. XRD patterns shown in Fig. 1(a and b) reveal the single-phase nature of $Ce_{1-x}Zr_xO_2$, varying from cubic to tetragonal structure with the Zr content. Fig. 1(c) displays a nearly linear relationship between the lattice parameters and the Zr content. The details can be seen in Table S1 in the ESI.† The observed change in the cell parameter with Zr contents is in agreement with Vegard's law and indicates the penetration of smaller Zr^{4+} cations into the ceria cubic lattice resulting in the formation of solid solutions in the whole doping range x = 0.25–0.75 by both FSP and CP methods. It is known that lattice strain, which represents a partially distorted lattice in a real crystal compared to the perfect structural model, originates from the lattice contraction and O_2 release followed by O_2^- vacancy production during the substitution process of Ce^{4+} ions by Zr^{4+} ions.[12] Thus, as observed in Fig. 1(d), the increase of the lattice strain with the Zr dopant content for CP-made samples indicates the enhancement of oxygen vacancy formation in high Zr content samples. In contrast, a slightly decreasing tendency is found in FSP-made samples. This reveals that O_2 release and OV formation are suppressed by the rapid quenching process, making the structure still close to the perfect model. And this suppression is more pronounced with higher incorporation of ZrO_2. This can also be seen from HRTEM images in Fig. S1† that the FSP-made sample exhibits an intermediate of the agglomeration of cubic-shaped particles in a high temperature calcination process, and the CP-made one seems like the final product.[23,24] This reveals that, in the FSP process, the oxides remain in a transition state as a result of instantaneous high temperature decomposition without long-time thermal treatment.

In general, the O_2 molecules are facile to be adsorbed at OVs and charged to form active oxygen species, such as superoxo (O_2^-) and/or peroxo species (O_2^{2-}).[25] It has been reported that electron paramagnetic resonance (EPR) lines observed in the g range between 2.047 and 2.009 can be attributed to paramagnetic species O_2^-.[26,27] The signals at g = 2.011 and g = 2.032 are assigned to surface-adsorbed O_2^- species bound to Ce^{4+} ions, which are capable of being transformed to O_2 molecules.[28] The EPR line with g = 2.047 is assigned to the superoxide O_2^- located in OVs. All of these signals appear in CP-made samples as shown in Fig. 2. In contrast, only a weak signal corresponding to OVs (g = 2.047) is observed for the FSP-made CeO_2 samples. This signal gets weaker with Zr addition and finally disappears, indicating that the FSP process dramatically suppresses the formation of oxygen vacancies especially for high Zr content. This result is consistent with the observed lattice strain tendency.

Investigation of lattice oxygen behaviour

As discussed above, the FSP-made Ce–Zr solid solution is in a metastable state without oxygen vacancies due to the quenching preparation process. The performance of oxygen release *via* breaking the metastable state is investigated through CO reduction, calcination, vacuum pretreatment and Au deposition.

Generally, a single sharp peak at about 465 cm^{-1} (F2g symmetry mode) in the Raman spectrum is usually used to

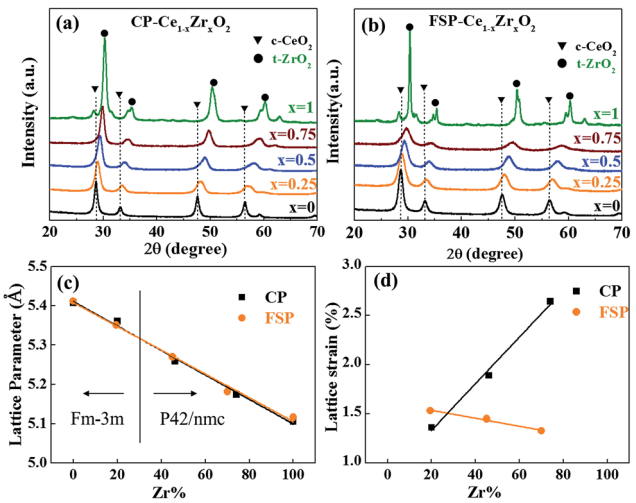

Fig. 1 X-ray diffraction patterns of Ce–Zr solid solutions made by CP (a) and FSP (b) methods. Lattice parameters (c) and lattice strain (d) are plotted against the Zr content.

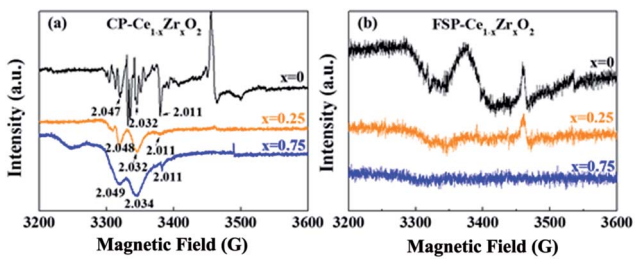

Fig. 2 EPR spectra of CP- (a) and FSP- (b) made $Ce_{1-x}Zr_xO_2$ samples collected at 100 K. The numbers marked at the peak represent g values.

characterize the surroundings of Ce^{4+} since it is very sensitive to oxygen sublattice disorder and nonstoichiometry.[29,30] It is observed from Fig. 3(A) that the F2g peaks broaden, diminish and become asymmetric with rising temperature for all tested samples. Simultaneously, a new broad feature appears at about 570 cm^{-1}, indicating the reduction of Ce^{4+} to Ce^{3+} and the formation of oxygen vacancies (OVs).[31] As we know, the precise assignment of OVs in Raman spectra is still controversial. It was reported that the peak at around 600–620 cm^{-1} was ascribed to OVs in Zr-doped CeO_2 in the literature.[32,33] Others assigned the OVs to 570 cm^{-1} in Raman spectra.[34–37] In the present *in situ* Raman investigation of FSP samples, the peaks appear at around 570 cm^{-1} and increase steadily with the increase of reduction temperature, while the peaks at around 600 cm^{-1} remain unchanged. This is a strong indication of OVs at around 570 cm^{-1}.

According to the literature, the Raman bands at *ca.* 600–620 cm^{-1} can be attributed to a nondegenerate Raman inactive Longitudinal Optical (LO) mode of ceria due to the substitution of zirconium into the ceria lattice.[38] The peak blue shift from 600 to 620 cm^{-1} can be observed with increasing Zr content, which may be attributed to the structural transformation from cubic to tetragonal. Weak bands at around 305 cm^{-1} can be attributed to the displacement of the oxygen atoms from their ideal fluorite lattice positions.[39] The enhancement of these bands with Zr content indicates the increasing disorder degree of oxygen atoms in the $Ce_{1-x}Zr_xO_2$ lattice. A new broad signal appears at around 260 cm^{-1} for $Ce_{0.25}Zr_{0.75}O_2$ samples and is assigned to the tetragonalization of the cubic structure.[32] According to the Raman spectra, tetragonalization is more strongly promoted by the inclusion of Zr in FSP-$Ce_{0.25}Zr_{0.75}O_2$ than in CP-$Ce_{0.25}Zr_{0.75}O_2$.

It can be seen from Fig. 3(B) that the amount of OVs created is much larger for FSP-made samples than for the corresponding CP-made ones, especially for the composition at $x = 0.75$. And the increasing rates with rising temperature are faster for the former than for the latter. For example, the ratio slightly increases and reaches 0.77 at 300 °C for CP-$Ce_{0.25}Zr_{0.75}O_2$. By contrast, it sharply goes up to 4.24 for FSP-$Ce_{0.25}Zr_{0.75}O_2$ even at a relatively low temperature (200 °C). This finding demonstrates that Ce reduction and oxygen vacancy formation are more accessible for FSP-made Ce–Zr oxide solid solutions. The Ce–O interaction is remarkably weakened by the FSP method, producing considerable active oxygen species. And the proportion of active oxygen species created in lattice oxygen around Ce^{4+} is more pronounced with increasing Zr content. It is also observed that the F2g signal of the FSP-$Ce_{0.25}Zr_{0.75}O_2$ sample becomes very small at 200 °C and is barely observed on further increasing the temperature, indicating that most of the Ce^{4+} ions on the surface can be reduced by CO under this condition. Note that no relations can be observed between oxygen release behaviors and the surface area which is listed in Table S1.† The oxygen release behaviors of CP-$Ce_{0.75}Zr_{0.25}O_2$ and FSP-$Ce_{0.75}Zr_{0.25}O_2$ samples are different although their surface areas are the same. Moreover, the amount of oxygen release increases with Zr content for FSP samples, while they possess the same surface area. Therefore, we suppose that the oxygen release behavior depends on the activity of lattice oxygen rather than the redox in the bulk phase. The catalytic performance in Fig. S2† exhibits that the formation of active oxygen species cannot be enhanced to infinity *via* increasing the Zr content since the Ce content is decreasing at the same time. In FSP-made samples, the amount of active oxygen species around Ce^{4+} is finally restricted by the Ce content, leading to a limited formation of OVs.

Peak shifts of the F2g mode for different gas flows and temperatures for FSP- and CP-made $Ce_{0.25}Zr_{0.75}O_2$ samples are shown as a bar diagram in Fig. 3(C). It shows that the F2g mode positions in He decrease with increasing temperature for both the tested samples. This red shift, which depends on temperature, is mostly attributed to thermal expansion as well as to phonon coupling and decay.[41] Compared to the CP-made samples, the F2g mode positions of FSP-$Ce_{0.25}Zr_{0.75}O_2$ at different temperatures are much lower due to mode softening, illustrating the enhancement of oxygen disorder. High static positional disorder can enhance the diffusivity and mobility of oxygen ions,[42] facilitating oxygen release. In addition, the bar reveals the change of the chemical environment from He to 2% CO/He atmosphere. The offsets of the F2g for the FSP-made

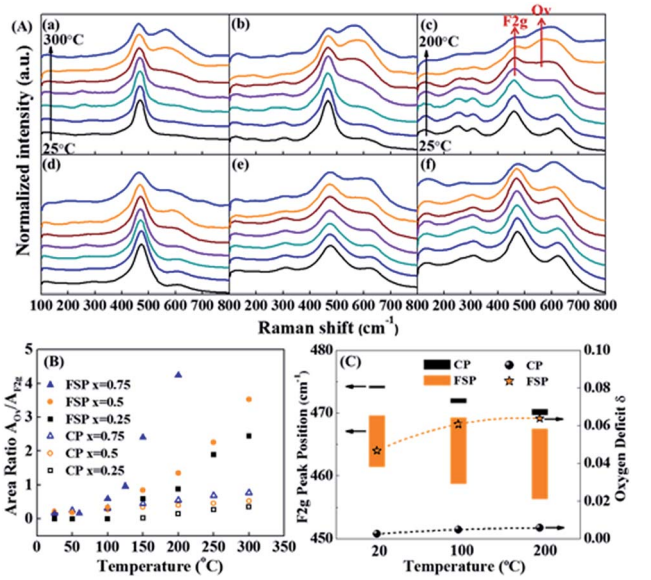

Fig. 3 (A) *In situ* Raman spectra of FSP- (a–c) and CP (d–f)-made $Ce_{1-x}Zr_xO_2$ in a 2% CO/He atmosphere, where (a and d) $x = 0.25$; (b and e) $x = 0.5$; and (c and f) $x = 0.75$. Note that the temperature of the FSP-$Ce_{0.25}Zr_{0.75}O_2$ sample (c) has been raised to 200 °C, while that of the others went up to 300 °C. (B) Variation of the peak area ratio of the oxygen vacancies (OVs) and Ce^{4+} (F2g) with rising temperature. The A_{Ov}/A_{F2g} ratio can be used as an indicator of the oxygen defect density compared to the existing Ce.[33,40] Therefore, the amount of OVs is only comparable between those samples with the same Ce content. (C) Downshifting of the F2g peak position of FSP- (orange) and CP (black)-made $Ce_{0.25}Zr_{0.75}O_2$ samples when the atmosphere changes from pure He to 2% CO/He at different temperatures and of their oxygen deficit δ, where the upper and lower limbs of the bar represent the F2g peak position in pure He and in 2% CO/He atmospheres, respectively. The length of the bar is the offset of F2g caused by exposure to a 2% CO atmosphere.

samples are much larger, exhibiting 8.2, 10.7 and 11.2 cm^{-1} at 20, 100 and 200 °C, respectively, compared to those for CP-made ones (0.5, 0.9 and 1.0 cm^{-1} corresponding to the same temperatures as above). It is reported that this additional downshifting with the CO flow is caused by lattice expansion or chemical strain.[41] It can be represented by $\Delta\omega = -\gamma\omega(\Delta V/V_0)$, where γ is the Grüneisen parameter (1.24),[43] and ΔV is the volume change from the reference case (He atmosphere) volume V_0. This fractional volume change of $Ce_{0.25}Zr_{0.75}O_{2-\delta}$ is a consequence of oxygen deficit δ formation, *i.e.* expansion due to the replacement of small Ce^{4+} (0.970 Å) ions by large Ce^{3+} (1.143 Å) ions, which is partially offset by effective compression owing to the loss of large O_2 (1.380 Å) and the creation of small OVs (1.164 Å). The oxygen deficit can be calculated by using the equation: $\delta = 2.66(\Delta\omega/\omega)$.[41] The δ values of the two samples, also shown in Fig. 3(C), exhibit an increasing trend with increasing temperature. The oxygen deficits of the FSP-$Ce_{0.25}Zr_{0.75}O_{2-\delta}$ sample are 0.0467, 0.0607 and 0.0622 at 20, 100 and 200 °C, respectively, which are more than one order of magnitude larger than those of CP-$Ce_{0.25}Zr_{0.75}O_{2-\delta}$ (0.0025, 0.0048 and 0.0057 at the same temperatures, respectively). It is worth noting that the amount of oxygen deficit of the FSP-made Ce–Zr oxide solid solution produced in the reductive atmosphere is extremely high, exceeding that of CeO_2 rods with Au deposition at 300 °C ($\delta = 0.039$),[41] considering that the rod shape, the existence of Au and high temperature are all positive factors for enhancing oxygen deficits. This demonstrates that the FSP preparation method is effective in softening the Ce–Zr oxide solid solution, enhancing the Ce^{4+} reducibility and facilitating the creation of large amounts of oxygen deficits. Thus, the oxygen release in the redox cycle is strengthened.

The formation of Ce–Zr oxide solid solutions with high oxygen activation ability in one step *via* the FSP method may be attributed to instantaneous high temperature and rapid quenching. The precursors directly decompose into oxide crystals in the flame at high temperature, and then the oxide particles quickly get away from the flame area. High temperature facilitates the formation of the crystal structure. Rapid quenching inhibits atomic rearrangement and the formation of strong metal–oxygen interactions. It also makes them stay in an intermediate state, leading to the O atoms lacking restriction and being released more readily. Therefore, long-time thermal treatment is executed in our work on the FSP-$Ce_{0.25}Zr_{0.75}O_2$ sample to break this state. From Fig. 4(A), it can be seen that a large amount of OVs is formed in FSP-$Ce_{0.25}Zr_{0.75}O_2$ at low temperature before the thermal treatment, indicating that the active oxygen atoms are easy to release and react with CO. However, no obvious OVs can be observed below 200 °C in the calcined sample, which is similar to the situation for CP-$Ce_{0.25}Zr_{0.75}O_2$. A sharp decrease of the peak area ratio (A_{Ov}/A_{F2g}) from 4.24 to 0.85 at 200 °C is found after the thermal treatment from Fig. 4(B). It can also be seen from Fig. 4(C) that the F2g peak positions in the 2% CO/He atmosphere increase from 456.3 to 467.2 cm^{-1} at 200 °C, and their deviation from those in the He atmosphere diminishes from 10.9 to 0.95 cm^{-1}. Meanwhile, the oxygen deficits decline from 0.0622 to 0.0054, representing that mode hardening happened during the thermal

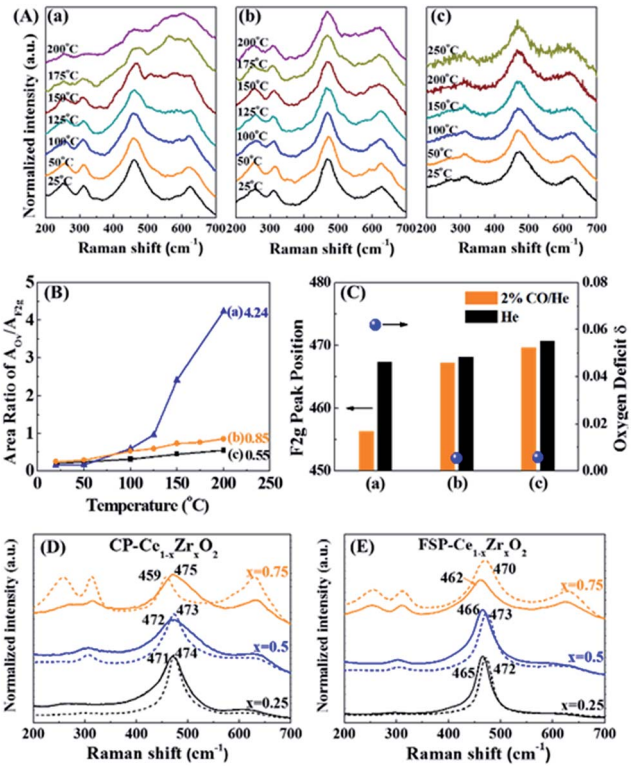

Fig. 4 (A) *In situ* Raman spectra in 2% CO/He of FSP-$Ce_{0.25}Zr_{0.75}O_2$ after calcination pretreatment at 800 °C for 3 h, where the Raman spectra of fresh FSP- and CP-made $Ce_{0.25}Zr_{0.75}O_2$ are also given for comparison. (B) Variation of the peak area ratio of oxygen vacancies (OVs) and Ce^{4+} (F2g) with rising temperature. (C) F2g peak position in He and 2% CO/He at 200 °C and oxygen deficit δ for FSP-$Ce_{0.25}Zr_{0.75}O_2$ (a), FSP-$Ce_{0.25}Zr_{0.75}O_2$–C (b) and CP-$Ce_{0.25}Zr_{0.75}O_2$ (c) samples. Raman spectra of calcination effects of CP (D)- and FSP (E)-made Ce–Zr oxide solid solutions with different Zr contents, where the solid and dashed lines refer to samples before and after calcination, respectively.

treatment. This makes the Ce–O bonding energy of FSP-$Ce_{0.25}Zr_{0.75}O_2$ increase and get close to that of CP-$Ce_{0.25}Zr_{0.75}O_2$, leading to a decrease of oxygen disorder degree. This also proves that the FSP-made Ce–Zr solid solutions stay in a metastable state owing to the rapid quenching. The crystals are produced and get away from the high-temperature zone in ultrashort time before the interactions among the atoms are strengthened. Subsequent long-time thermal treatment will transform the chemical bonds from metastable to stable states, leading to relatively hard oxygen release and low oxygen activation ability, which is similar to that observed in CP-made samples.

The influence of thermal treatment on the F2g peak is observed from Fig. 4(D and E) by narrowing the line, increasing its symmetry and moving it to a higher Raman shift, which may be related to the rearrangement of atoms during the calcination process. Note that no obvious variations can be detected in morphology, particle size or phase from Fig. S3 and S4.† The effect of particle size on the Raman peak position can be excluded.[44] Compared to fresh CP-made ones, about 5 to 13 cm^{-1} (Table S2†) lower F2g peak position is found with Zr content increasing from 25 to 75% for fresh FSP-made samples.

However, these gaps disappear, *i.e.*, the peak positions are getting close to those of the fresh CP-made ones after thermal treatment at 800 °C. The F2g downward shift and the presence of a new peak at 258 cm^{-1} of CP-$Ce_{0.25}Zr_{0.75}O_2$ indicate the phase transformation.[12] The degree of oxygen disorder can be strengthened by the quenching process in FSP. And this effect is more pronounced in the samples with high Zr content and can be diminished through high temperature thermal treatment.

XPS studies are performed in order to analyze oxygen release and OV formation during vacuum treatment *via* measuring the amount of surface Ce^{3+}/Ce ratio. In Fig. 5, XPS Ce 3d signals of catalysts show eight peaks corresponding to the spin–orbit doublet (SOD) and satellite lines characteristic of Ce in the oxidized state.[45] It is clearly shown in Table S3† that Ce^{3+}/Ce surface atomic ratios of FSP-made catalysts are higher than those of the corresponding CP-made ones. In particular, the ratios of FSP-$Ce_{0.25}Zr_{0.75}O_2$ and CP-$Ce_{0.25}Zr_{0.75}O_2$ are 0.24 and 0.17, respectively. According to EPR results, no sign of oxygen vacancy existence can be found in FSP-$Ce_{0.25}Zr_{0.75}O_2$. It can be supposed that about 24% of Ce^{4+} turn into Ce^{3+} due to oxygen release during vacuum treatment, far exceeding that observed in the CP-made one. This indicates that the surface lattice oxygen is more readily released for the former than the latter.

Fig. 6(A and B) show the effect of Au deposition on the Raman spectra of Ce–Zr oxide solid solutions. In contrast to the calcination effect, Au deposition will broaden the F2g peaks and lead to a red shift ranging from 8.2 to 12.6 cm^{-1} and from 12.6 to 29.6 cm^{-1} for CP- and FSP-made samples, respectively, as shown in Table S4.† Au deposition has a more remarkable effect on the enhancement of oxygen distortion for FSP-made catalysts by weakening the Ce–O interaction which makes the oxygen atoms more accessible. In particular, a clear Raman shift from 461.7 to 432.1 is observed for the Au/FSP-$Ce_{0.25}Zr_{0.75}O_2$ catalyst. At the same time, a Raman peak at 570 cm^{-1}, which is assigned to OVs, appears accompanied by a decrease of the F2g peak area. This phenomenon is also observed from EPR as shown in Fig. 6(C). The paramagnetic signals of O_2^- located in OVs are strengthened after Au deposition for FSP-made samples. Furthermore, the TPR results in Fig. 6(D) show that distorted oxygen atoms from FSP-$Ce_{0.25}Zr_{0.75}O_2$ can easily detach from the metal oxide constraint at room temperature with the assistance of Au. This can be attributed to the strong

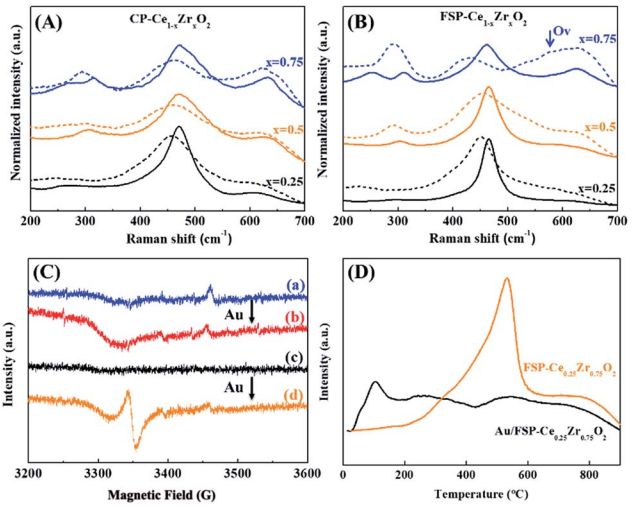

Fig. 6 Raman spectra of Au deposition effects of CP (A)- and FSP (B)-made Ce–Zr oxide solid solutions with different Zr contents, where the solid and dashed lines refer to samples before and after Au deposition, respectively. (C) EPR spectra of (a) FSP-$Ce_{0.75}Zr_{0.25}O_2$; (b) Au/FSP-$Ce_{0.75}Zr_{0.25}O_2$; (c) FSP-$Ce_{0.25}Zr_{0.75}O_2$; and (d) Au/FSP-$Ce_{0.25}Zr_{0.75}O_2$. (D) TPR results of FSP-$Ce_{0.75}Zr_{0.25}O_2$ before and after Au deposition.

interaction of Au with Ce ions, which may further weaken the Ce–O bonds and lower the OV formation energy.[46] The OVs at the Au–support interface will also promote the oxygen mobility and facilitate the reduction. TPR results of the other samples are shown in Fig. S6.† Compared to the CP method, the application of FSP makes the Ce^{4+} reduction temperature of Ce–Zr oxide solid solutions decline by about 40–80 °C. And the reduction starting point is decreased from 300 to 250 °C. Although Au deposition can dramatically enhance the surface Ce^{4+} reduction, a large portion of Ce^{4+} is still reduced at high temperature in CP-made samples. Therefore, we propose that the oxygen release and the creation of OVs preferentially happen at the interface between Au and the support. The OVs created at the interface are the active sites in the CO oxidation reaction due to the promotion of oxygen mobility.[47,48]

From previous analysis, the schematic diagram of oxygen behaviour is proposed in Fig. 7. The distorted oxygen atoms of metastable Ce–Zr oxide solid solutions are released readily in

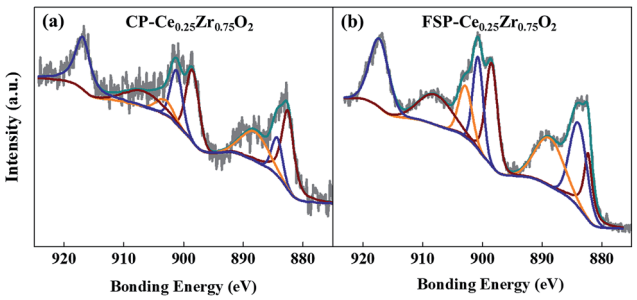

Fig. 5 XPS spectra in Ce 3d of CP (a) and FSP (b) made $Ce_{0.25}Zr_{0.75}O_2$ catalysts; the spectra of the other samples and the details of peak fitting results can be seen in Fig. S5 and Table S3,† respectively.

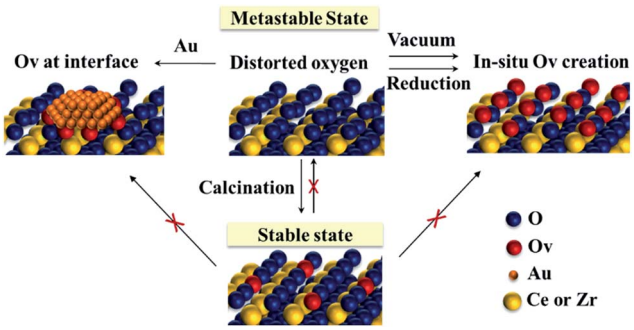

Fig. 7 Schematic diagram of the oxygen behaviour of the metastable Ce–Zr oxide solid solution under different conditions.

Table 1 Fundamental properties and activity of CeO_2 with various morphologies and Ce–Zr oxide solid solutions with different Zr contents as supports for Au catalysts in CO oxidation[a]

Supports	Oxides prep.	Au prep.	Au loading[b] (wt%)	Reaction rate[c] (mol CO/g_{Au} h)	Ref.
CeO_2-nanorod	HT	DP	0.98	4.02	49
CeO_2-cubic	CP	DP	0.94	0.15	49
CeO_2-cubic	CP	DP	1.0	1.67	50
CeO_2-flowerlike	HT	DP	2.77	0.05	51
$Ce_{0.75}Zr_{0.25}O_2$	Sol–gel	DAE	1.68	0.45	52
$Ce_{0.5}Zr_{0.5}O_2$	Sol–gel	DAE	1.74	0.10	52
$Ce_{0.25}Zr_{0.75}O_2$	Sol–gel	DAE	1.71	0.03	52
$Ce_{0.75}Zr_{0.25}O_2$	Sol–gel	DP	1.01	2.89	32
$Ce_{0.5}Zr_{0.5}O_2$	Sol–gel	DP	0.92	4.05	32
$Ce_{0.75}Zr_{0.25}O_2$	FSP	DP	0.94	3.79	PW
$Ce_{0.5}Zr_{0.5}O_2$	FSP	DP	0.95	6.47	PW
$Ce_{0.25}Zr_{0.75}O_2$	FSP	DP	0.90	7.28	PW
$Ce_{0.75}Zr_{0.25}O_2$	CP	DP	0.91	2.14	PW
$Ce_{0.5}Zr_{0.5}O_2$	CP	DP	1.06	2.09	PW
$Ce_{0.25}Zr_{0.75}O_2$	CP	DP	0.52	0.76	PW

[a] Abbreviations: HT, hydrothermal; DP, deposition precipitation; NR, not reported; DAE, direct anionic exchange; PW, present work. [b] Measured by ICP-OES. [c] Specific reaction rate of CO oxidation at low conversions in a kinetically controlled regime at room temperature.

the reduction atmosphere or under vacuum treatment, *in situ* producing plenty of OVs and supplying a considerable amount of active oxygen species. They can accelerate the redox cycles and enhance the oxygen activation. Besides, the creation of OVs preferentially happens at the interface between Au and the support during Au deposition, which promotes the oxygen atom mobility and their reaction with the activated CO molecule. Therefore, it is supposed that the redox properties are determined by the rate of oxygen release rather than the existing oxygen vacancies. However, long-time thermal treatment at high temperature (above 800 °C) can break the metastable state. The distorted oxygen atoms will rearrange with OV formation during calcination. This could bring the oxides into a stable state, where it is then hard to supply more active oxygen in the process of reaction.

Catalytic performance in CO oxidation

It is reported that the optimal catalyst composition has been analysed by a temperature scanning method (TSM) based on the experimental data of CO oxidation for a series of Au/$Ce_{1-x}Zr_xO_2$ (x = 0, 0.25, 0.5, 0.75, and 1) catalysts and identified to be x = 0.25.[53] Regular behaviour has been reported that Ce–Zr oxide solid solutions with extremely high Zr content (higher than 60%) exhibit low redox activity due to the formation of a non-defective t phase.[12] The CO oxidation reaction rates over Ce–Zr oxide solid solutions reported in the literature and in our work are summarized in Table 1. It can be found that the CO reaction rate obviously increases with the Zr content for the FSP-made samples, which is in contrast to that for CP-made ones and has never been reported before. The activity of the Au/FSP-$Ce_{0.25}Zr_{0.75}O_2$ sample is much higher than that of the most active ones employed in the literature, including allotropic ceria and Ce–Zr oxide solid solutions. Generally, Zr addition leads to structure relaxation in the lattice, decreasing the oxygen vacancy formation energy[54] and promoting the oxygen mobility. However, the Ce–O bond length becomes shorter with Zr doping into the CeO_2 framework, which could suppress oxygen release.[55] Simultaneously, the amount of oxygen bonding with Ce decreases with increasing Zr content. This can explain why the Zr content always has an optimum value. The usage of the quenching method for producing Ce–Zr oxide solid solutions could weaken the Ce–O interaction and activate oxygen atoms around Ce, which compensates the negative effect of Ce reduction. This makes its oxygen activation capability stay at a high level even for low Ce content.

The activation energy of CP- and FSP-made Au/$Ce_{1-x}Zr_xO_2$ has been tested in the CO oxidation reaction while keeping the CO conversion below 20%. The activation energy of all samples is almost unchanged, fluctuating in the range of 39.1 to 41.1 kJ mol^{-1}. This indicates that the reaction mechanism is the same for both catalysts, including the same rate-determining step and similar energy potential diagrams. The improvement in the catalytic activity of CO oxidation lies in that the FSP catalyst can supply more active sites than the CP one.

Conclusions

Rapid quenching from extremely high temperature can freeze Ce–Zr oxide solid solutions in a metastable state with highly disordered oxygen, which results in an enhancement of the capability for oxygen release. A reduction atmosphere can induce 19 times more oxygen deficit formation from FSP-$Ce_{0.25}Zr_{0.75}O_2$ than the corresponding CP-made one at room temperature. The lattice oxygen atoms readily detach from the constraint of metals in the vacuum treatment, producing large amounts of OVs. Besides, during Au deposition, the creation of OVs preferentially happens at the interface between Au and the support. CO oxidation reaction rates obviously increase with the Zr content for Au/FSP-$Ce_{1-x}Zr_xO_2$, which is in contrast to conventional CP-made samples and has never been reported before. The quenching method used in our work has proved to

be effective in enhancing oxygen release and accelerating redox cycles. Foreseeably, this new concept can be widely employed in many oxygen activation reactions in heterogenous catalysis.

Conflicts of interest

There are no conflicts to declare.

Acknowledgements

The research has received funding from the Helmholtz Association of German Research Centre and the Chinese Academy of Sciences (CAS) Joint Research Group (Grants HCJRG 118 and GJHZ1304). The authors would like to acknowledge Dr Jinsuo Gao for his help in EPR measurements. We also appreciate Dr Teng He for his efforts in *in situ* Raman characterizations. Dr Jian Sun would like to thank the support of the Youth Innovation Promotion Association of CAS.

Notes and references

1 X. Y. Liu, A. Wang, T. Zhang and C.-Y. Mou, *Nano Today*, 2013, **8**, 403–416.
2 R. W. McCabe and A. Trovarelli, *Appl. Catal., B*, 2016, **197**, 1.
3 Q. Fu, H. Saltsburg and M. Flytzani-Stephanopoulos, *Science*, 2003, **301**, 935–938.
4 D. Widmann and R. J. Behm, *Accounts Chem. Res.*, 2014, **47**, 740–749.
5 A. Ruiz Puigdollers, P. Schlexer, S. Tosoni and G. Pacchioni, *ACS Catal.*, 2017, **7**, 6493–6513.
6 H. Tsuji and H. Hattori, *ChemPhysChem*, 2004, **5**, 733–736.
7 R. Kopelent, J. A. van Bokhoven, J. Szlachetko, J. Edebeli, C. Paun, M. Nachtegaal and O. V. Safonova, *Angew. Chem., Int. Ed.*, 2015, **54**, 8728–8731.
8 M. H. Takashi Fujita, T. Takei, T. Murayama and M. Haruta, *Chin. J. Catal.*, 2016, **37**, 1651–1655.
9 N. N. Bulgakov, V. A. Sadykov, V. V. Lunin and E. Kemnitz, *React. Kinet. Catal. Lett.*, 2002, **76**, 103–110.
10 M. Piumetti, S. Bensaid, N. Russo and D. Fino, *Appl. Catal., B*, 2015, **165**, 742–751.
11 M. Piumetti, S. Bensaid, D. Fino and N. Russo, *Appl. Catal., B*, 2016, **197**, 35–46.
12 R. Si, Y.-W. Zhang, S.-J. Li, B.-X. Lin and C.-H. Yan, *J. Phys. Chem. B*, 2004, **108**, 12481–12488.
13 M. Yashima, *Catal. Today*, 2015, **253**, 3–19.
14 L. Mädler, H. K. Kammler, R. Mueller and S. E. Pratsinis, *J. Aerosol Sci.*, 2002, **33**, 369–389.
15 T. R. Hinklin, J. Azurdia, M. Kim, J. C. Marchal, S. Kumar and R. M. Laine, *Adv. Mater.*, 2008, **20**, 1373–1375.
16 T. R. Hinklin and R. M. Laine, *Chem. Mater.*, 2008, **20**, 553–558.
17 S. T. Murphy, C. A. Gilbert, R. Smith, T. E. Mitchell and R. W. Grimes, *Philos. Mag.*, 2010, **90**, 1297–1305.
18 R. Strobel, M. Maciejewski, S. E. Pratsinis and A. Baiker, *Thermochim. Acta*, 2006, **445**, 23–26.
19 W. Y. Teoh, R. Amal and L. Madler, *Nanoscale*, 2010, **2**, 1324–1347.
20 G. A. Kelesidis, E. Goudeli and S. E. Pratsinis, *Proc. Combust. Inst.*, 2017, **36**, 29–50.
21 R. Strobel, F. Krumeich, W. J. Stark, S. E. Pratsinis and A. Baiker, *J. Catal.*, 2004, **222**, 307–314.
22 H. L. Tang, J. K. Wei, F. Liu, B. T. Qiao, X. L. Pan, L. Li, J. Y. Liu, J. H. Wang and T. Zhang, *J. Am. Chem. Soc.*, 2016, **138**, 56–59.
23 J. P. Y. Tan, H. R. Tan, C. Boothroyd, Y. L. Foo, C. B. He and M. Lin, *J. Phys. Chem. C*, 2011, **115**, 3544–3551.
24 A. Trovarelli and J. Llorca, *ACS Catal.*, 2017, **7**, 4716–4735.
25 X.-M. Zhang, Y.-Q. Deng, P. Tian, H.-h. Shang, J. Xu and Y.-F. Han, *Appl. Catal., B*, 2016, **191**, 179–191.
26 C. Oliva, G. Termignone, F. P. Vatti, L. Forni and A. V. Vishniakov, *J. Mater. Sci.*, 1996, **31**, 6333–6338.
27 X. Zhang and K. J. Klabunde, *Inorg. Chem.*, 1992, **31**, 1706–1709.
28 E. Abi-aad, R. Bechara, J. Grimblot and A. Aboukais, *Chem. Mater.*, 1993, **5**, 793–797.
29 M. Yashima, H. Arashi, M. Kakihana and M. Yoshimura, *J. Am. Ceram. Soc.*, 1994, **77**, 1067–1071.
30 W. H. Weber, K. C. Hass and J. R. McBride, *Phys. Rev. B*, 1993, **48**, 178–185.
31 G. Gouadec and P. Colomban, *Prog. Cryst. Growth Charact. Mater.*, 2007, **53**, 1–56.
32 O. H. Laguna, A. Pérez, M. A. Centeno and J. A. Odriozola, *Appl. Catal., B*, 2015, **176–177**, 385–395.
33 O. H. Laguna, F. Romero Sarria, M. A. Centeno and J. A. Odriozola, *J. Catal.*, 2010, **276**, 360–370.
34 D. W. Wheeler and I. Khan, *Vib. Spectrosc.*, 2014, **70**, 200–206.
35 H. Li, P. Zhang, G. Li, J. Lu, Q. Wu and Y. Gu, *J. Alloy. Comp.*, 2016, **682**, 132–137.
36 Z. Wang, Q. Wang, Y. Liao, G. Shen, X. Gong, N. Han, H. Liu and Y. Chen, *ChemPhysChem*, 2011, **12**, 2763–2770.
37 A. B. Hungría, A. Martínez-Arias, M. Fernández-García, A. Iglesias-Juez, A. Guerrero-Ruiz, J. J. Calvino, J. C. Conesa and J. Soria, *Chem. Mater.*, 2003, **15**, 4309–4316.
38 B. M. Reddy, P. Lakshmanan, A. Khan, S. Loridant, C. López-Cartes, T. C. Rojas and A. Fernández, *J. Phys. Chem. B*, 2005, **109**, 13545–13552.
39 B. M. Reddy, P. Bharali, P. Saikia, S.-E. Park, M. W. E. van den Berg, M. Muhler and W. Grünert, *J. Phys. Chem. C*, 2008, **112**, 11729–11737.
40 Y. Li, Z. Wei, F. Gao, L. Kovarik, R. A. L. Baylon, C. H. F. Peden and Y. Wang, *ACS Catal.*, 2015, **5**, 3006–3012.
41 Y. Lee, G. He, A. J. Akey, R. Si, M. Flytzani-Stephanopoulos and I. P. Herman, *J. Am. Chem. Soc.*, 2011, **133**, 12952–12955.
42 M. Yashima and T. Wakita, *Appl. Phys. Lett.*, 2009, **94**, 171902.
43 J. R. McBride, K. C. Hass, B. D. Poindexter and W. H. Weber, *J. Appl. Phys.*, 1994, **76**, 2435–2441.
44 F. Zhang, S.-W. Chan, J. E. Spanier, E. Apak, Q. Jin, R. D. Robinson and I. P. Herman, *Appl. Phys. Lett.*, 2002, **80**, 127–129.
45 J. A. Hernández, S. A. Gómez, T. A. Zepeda, J. C. Fierro-González and G. A. Fuentes, *ACS Catal.*, 2015, **5**, 4003–4012.

46 A. Ruiz Puigdollers, P. Schlexer, S. Tosoni and G. Pacchioni, *ACS Catal.*, 2017, **7**, 6493–6513.
47 M. Haruta, *Chem. Rec.*, 2003, **3**, 75–87.
48 L. Li, A. Wang, B. Qiao, J. Lin, Y. Huang, X. Wang and T. Zhang, *J. Catal.*, 2013, **299**, 90–100.
49 X.-S. Huang, H. Sun, L.-C. Wang, Y.-M. Liu, K.-N. Fan and Y. Cao, *Appl. Catal., B*, 2009, **90**, 224–232.
50 L.-H. Chang, N. Sasirekha, B. Rajesh and Y.-W. Chen, *Sep. Purif. Technol.*, 2007, **58**, 211–218.
51 C. Sun, H. Li and L. Chen, *J. Phys. Chem. Solids*, 2007, **68**, 1785–1790.
52 I. Dobrosz-Gómez, I. Kocemba and J. M. Rynkowski, *Appl. Catal., B*, 2008, **83**, 240–255.
53 M.-Á. Gómez-García, N. A. Gómez Mendoza, I. Dobrosz-Gómez, E. GilPavas and J. Rynkowski, *Chem. Eng. J.*, 2015, **282**, 20–28.
54 J. Paier, C. Penschke and J. Sauer, *Chem. Rev.*, 2013, **113**, 3949–3985.
55 G. Vlaic, R. Di Monte, P. Fornasiero, E. Fonda, J. Kašpar and M. Graziani, *J. Catal.*, 1999, **182**, 378–389.